J. Fluid Mech. (1992), *vol.* 241, *pp.* 587–614
Printed in Great Britain

Plane turbulent jets in a bounded fluid layer

By T. DRACOS[1], M. GIGER[1] AND G. H. JIRKA[2]

[1] Swiss Federal Institute of Technology, Zürich, 8093 Zürich, Switzerland

[2] Cornell University, Ithaca NY 14853, USA

(Received 14 August 1989 and in revised form 22 January 1992)

An experimental investigation of plane turbulent jets in bounded fluid layers is presented. The development of the jet is regular up to a distance from the orifice of approximately twice the depth of the fluid layer. From there on to a distance of about ten times the depth, the flow is dominated by secondary currents. The velocity distribution over a cross-section of the jet becomes three-dimensional and the jet undergoes a constriction in the midplane and a widening near the bounding surfaces. Beyond a distance of approximately ten times the depth of the bounded fluid layer the secondary currents disappear and the jet starts to meander around its centreplane. Large vortical structures develop with axes perpendicular to the bounding surfaces of the fluid layer. With increasing distance the size of these structures increases by pairing. These features of the jet are associated with the development of quasi two-dimensional turbulence. It is shown that the secondary currents and the meandering do not significantly affect the spreading of the jet. The quasi-two-dimensional turbulence, however, developing in the meandering jet, significantly influences the mixing of entrained fluid.

1. Introduction

In the present work we consider a fluid layer bounded by two parallel surfaces with a separation distance H, simply called the depth of the fluid layer. The bounding surfaces may be shear-supporting (no-slip) or shear-free. The fluid layer receives a high velocity discharge through a slot of width B that extends over the full depth H, and an aspect ratio $H/B \gg 1$. A plane turbulent jet with a Reynolds number $Re_0 = U_0 B/\nu > 10^3$, where U_0 is the exit velocity and ν the kinematic viscosity, is generated in the fluid layer. The evolution of this jet flow for large streamwise distances, for which the jet half-width b exceeds the depth, $b/H > 1$, is the subject of this study.

There have been very few investigations into the behaviour of plane jets that occupy the region $x/H \gg 1$. The absence of detailed studies of 'shallow-free jets' and their large distance evolution, $x/H \gg 1$, is particularly surprising as these conditions are, in fact, the standard case in many geophysical and environmental engineering applications. Industrial effluents, e.g. cooling water discharges or natural rivers issuing into shallow lakes or into the upper layer of deep lakes bounded below by a thermocline or into the coastal shelf zone, are all in the category $x/H \gg 1$, with values ranging up to 100 and beyond. Tidal jets due to the periodic emptying of a coastal lagoon are another case, as are topographically induced jets in the stratified atmosphere.

Foss & Jones (1968) and Holdemann & Foss (1975) studied shallow jets in fluidic switching devices in the limited range $x/H \leqslant 10$. They found that secondary flow

structures develop at some distance from the orifice and attribute them to vortex interaction between the free shear layers and the wall shear layers. In their experiments conducted with $H/B = 4$ these secondary flows seem to be fully decayed at a distance $x/B \approx 40$. Beyond that distance the jet seems to return to the usual two-dimensional flow condition of a plane jet with a relatively thin boundary layer near the plates (Holdemann & Foss 1975).

Usually, in studies of two-dimensional turbulent plane jets the effects of the bounding surfaces are undesirable. Measurements are therefore mostly limited to a distance from the orifice of the order of the separation between the bounding walls, i.e. $x/H \sim 1$. In the absence of wall effects and beyond an initial zone of flow establishment, a jet in self-preserving state begins to form. For such a jet an invariant local force equilibrium exists. All its properties, including turbulence intensities, can then be uniquely scaled with local variables, and the equations of motion can be simplified by using similarity techniques as shown by the early works of Tollmien (1926), Görtler (1942) and Reichardt (1942).

The structure of the turbulence in the self-preserving zone of two-dimensional jets has been measured in a number of studies (e.g. Bradbury 1965; Goldschmidt & Young 1975; Gutmark & Wygnanski 1976; Everitt & Robins 1978; Bashir & Uberoi 1975; Ramaprian & Chandrasekhara 1983). The turbulence in these flows is characterized by the three-dimensional vortex stretching mechanism and exhibits an equilibrium range with a $-\frac{5}{3}$ wavenumber dependence in the power spectrum. The dominant energy-containing eddies appear to be those typical for shear flow, that is to say, they have principal axes aligned with those of the mean strain rate (Townsend 1976), even though there is disagreement about their exact geometry and orientation (e.g. Moum, Kawall & Keffer 1979; Mumford 1982). The ratio of integral scale to velocity half-width is estimated to be about 0.3 (Bradbury 1965) to 0.5 (Goldschmidt & Bradshaw 1981).

Coherent structures within the plane jet have their origin in the unstable mixing layers that develop immediately downstream from the efflux. The nonlinear growth, two-dimensional interaction (pairing) and three-dimensional secondary instabilities in such mixing layers have been convincingly demonstrated (e.g. Winant & Browand 1974; Jimenez 1983).

For sufficiently large distances and for high Reynolds numbers (Foss 1977; Hussain & Zedan 1978) the structures are generally imbedded into, and interacting with, the three-dimensional turbulence field of the mixing layers and – after their lateral merging – of the plane jet. Their detection and eduction then becomes a matter of considerable art and subjectivity leading to frequently contradictory conclusions. Reliable experimental methods are still evolving. Two-point velocity correlations on opposite jet sides by Cervantes & Goldschmidt (1983) showed an apparent flapping motion, which was attributed to local (apparently two-dimensional) coherent structures within the jet's turbulence field (see also Mumford 1982). More detailed spatial correlation measurements by Oler & Goldschmidt (1982) and visualizations by Goldschmidt, Moallemi & Oler (1983) suggest a 'two-dimensional vortex street' structure. Space–time correlations of velocity and of tracer fluctuations by Antonia *et al.* (1983) also demonstrated the existence of spanwise counter-rotating structures. In contrast, measurements by Moum *et al.* (1979, 1983) supported the occurrence of large-scale 'randomly occurring' coherent structures, but found no correlation between opposite sides. Hussain (1983), in turn, detected three-dimensional structures that have both streamwise and spanwise vorticities quite different from the ones of other studies. Recent work by Thomas & Goldschmidt (1986) gives

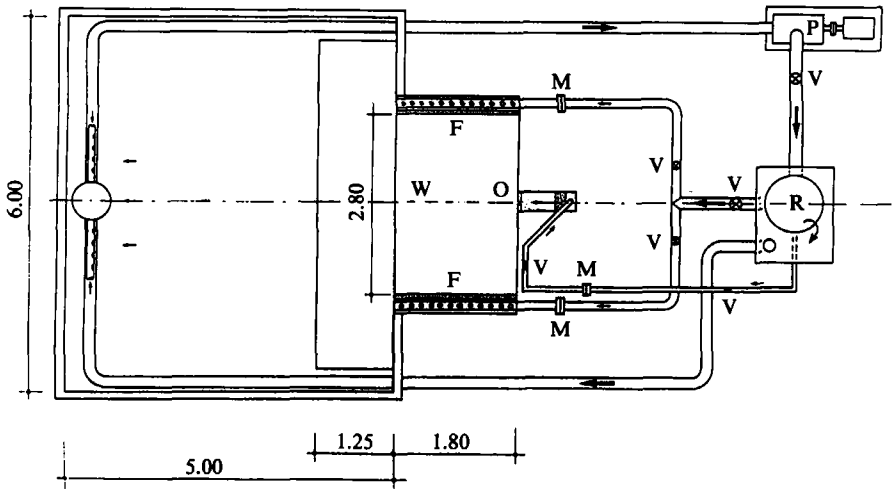

FIGURE 1. Schematic plane view of experimental set-up. W, water table; P, pump; R, constant head reservoir; V, valves; O, jet-orifice; F, lateral feeders; M, flowmeters. Dimensions are given in metres.

further evidence for the co-existence of different structure types in the downstream region of the plane jet.

In short, available evidence suggests that the two-dimensional turbulent jet, in the absence of effects of the third dimension, i.e. in practice, for $x/H < 1$, is in the main governed by a three-dimensional vorticity transfer mechanism with a well-established equilibrium range. Furthermore, large-scale organized motions seem to occur, but considerable uncertainty exists with regard to their spatial and temporal structures.

In contrast to the existing body of knowledge on plane turbulent jets, in which the influence of the bounding surface is either absent or minimal, the present study on jets in shallow fluid layers demonstrates flow behaviour that differs in many aspects, often radically so. Section 2 provides a description of the experimental apparatus. A new subdivision of the plane jet into a near, middle and far field, which is based on the depth as a scaling parameter, is introduced in §3 of this paper. Mean flow properties of the shallow jet in the near, middle and far field are summarized in §4. The turbulent structure in the far field ($x/H \geqslant 10$) (§5) is dominated by two-dimensional large-amplitude quasi-periodic motions which give it the appearance of a 'meandering jet'. Spectral and intermittency characteristics of the flow are provided in §§ 6 and 7.

2. Experimental apparatus

Figure 1 shows a schematic sketch of the experimental apparatus. The experiments were conducted on a horizontal water table with a streamwise extent of 1.80 m and a width of 2.8 m. At the downstream end, the water table is open to a large receiving basin of 5 m × 6 m with a depth of 1 m. A flat horizontal plate extends the water table an additional 1.25 m into this basin so that the total longitudinal distance over which the shallow jet can be observed is 3.05 m.

The water jet was discharged through a vertical slot which issues at the upstream end of the water table. In all experiments performed the slot width B was equal to

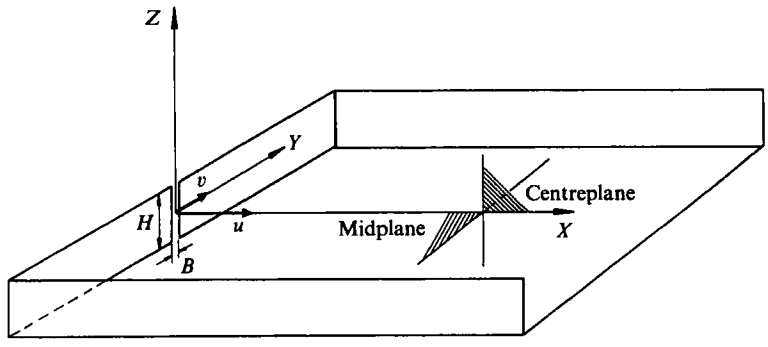

FIGURE 2. Definition sketch for plane jet into bounded fluid layer.

1 cm and the jet had a nominal exit velocity of 110 cm/s resulting in a Reynolds number of about 10^4 at the orifice. Two different nozzles were used. The first nozzle was bottle-shaped with a contraction of 10:1. The downstream end of the nozzle consisted of a 10 mm long section with parallel sidewalls. The contraction ratio of the second nozzle was 22:1. It was achieved by a single curvature of 10 mm radius. Pressure measurements showed that a vena contracta did not occur after either of the two nozzles. The height of the slot was equal to the water depth H over the water table. This depth was varied in the range 20–360 mm or $H/B = 2$–36. A glass plate forms the bottom of the water table while the top is provided by another removable glass plate or simply by the shear-free water surface.

Definitions and notations used in this study are shown in figure 2. Jet entrainment induces a potential flow in the receiving fluid body. Theoretically, this fluid body should have an infinite lateral extent. To approximately satisfy this condition in the laterally confined water table, water was supplied on both sides of the table through perforated pipes at a rate corresponding to the estimated entrainment rate. The flow field in the receiving water body was visualized and compared with Taylor's solution (Taylor 1958) for the flow induced by the entrainment of the jet. The agreement was excellent. This investigation was carefully carried out before starting the proper measurements and showed that an influence of the lateral discharge supply on the jet flow can be excluded in the range of the operating conditions of the experiments conducted in this facility (for more details see Giger 1987; Giger, Dracos & Jirka 1991). The sum of the jet discharge and the lateral feeding flow was withdrawn at the downstream end of the main basin in order to maintain a constant water level.

Flow visualizations were made by means of dye continuously injected into the jet efflux. Additionally, confetti was put on the free surface in some experiments. Photographic observations were carried out by a single-picture camera or a movie camera mounted overhead.

Velocity measurements were performed using laser-Doppler anemometry (LDA) with a vertical beam alignment for the two horizontal velocity components u and v. A special LDA platform was constructed with the emitting optics located below the water table and the receiving optics above. A 15 mW helium–neon–laser was used as light source. Two focusing lenses with a nominal focusing distance of 200 and 300 mm were used alternatively to focus the three light beams in a measuring volume. Movement of the platform allowed three-dimensional positioning of the measuring volume. This volume had a vertical dimension of 1.8 mm and a horizontal one of 0.07 mm for the first lens, and 4.0/0.15 mm respectively for the second lens. The frequency shift necessary for a correct determination of the sign of the velocity

vector was accomplished by a rotating optical grid. Imperfection of the grid resulted in a periodic ripple superimposed on the measuring signal. The use of a phase-locked loop enabled a synchronous sampling so that the negative effect of this ripple could be reduced to a minimum. A tracker was used to process the Doppler signal. The angle formed by two of the laser light beams in each of the two measuring planes and a proportionality constant are needed to compute the two velocity components from the measured signals. These constants were determined by a special calibration procedure, which was repeated periodically during the measurements. For more details of the LDA system used see Müller (1980).

The data were low-pass filtered at a cut-off frequency of 100 Hz, sampled through an 11-bit A/D-converter at a rate of 212 Hz and digitally recorded. The whole process was controlled by a PDP-11/34 computer. The measuring time was variable in streamwise distance and increased according to the similarity law of the plane jet from 60 s at $x/B = 20$ to 1200 s at $x/B = 153$. The rough data were stored first on RK05-disc and then transferred to a VAX-8650 computer for further processing.

3. The depth as scaling parameter for the flow classification in shallow plane jets

Figure 3(*a*) shows a dimensionless distribution of the turbulence intensity of the u-velocity component versus the streamwise distance x. The local mean velocity U_m on the jet axis was chosen as the scaling velocity. The abscissa was scaled in the usual way with the slot width B since it is the appropriate length scale for a two-dimensional jet, namely $\xi = x/B$. Data are shown for the experiments described in the present work and from the study of Holdemann & Foss (1975). The experiments differ only in the water depth H. The data of each experiment follow different curves. With the exception of the experiment with $H/B = 4$, these curves show a common general trend: an initial increase in the intensity ends in a peak followed by a subsequent decrease down to a more or less constant plateau. Figure 3(*b*) shows the same sets of data, but with the abscissa scaled with H instead of B. This scaling makes the data collapse onto a single curve. They show some scatter, but have a peak near $\xi' = 6$, and the constant plateau begins near $\xi' = 10$. Beyond that point, the data of the experiment with $H/B = 4$ coincide with the data of the other experiments. When scaled the same way, the data of Holdemann & Foss (1975) show the same trend and are in reasonable agreement with the data of the present work.

From figure 3(*b*) it is concluded that the streamwise turbulent intensity is approximately constant for distances greater than about 10 times the depth H. The level of the turbulence intensity for $\xi' > 10$, where $\xi' = x/H$, is close to 0.2. The region $\xi' < 10$ is influenced by a pronounced secondary flow of the second type. Foss & Jones (1968) and Holdemann & Foss (1975) have performed comprehensive measurements in this zone. The main effect of the secondary currents consists in a transport of fast jet fluid from the axis towards the boundaries along the centreplane and of slow ambient fluid towards the axis of the jet along the midplane. This transport causes a deficit of momentum flux in the midplane. For this reason the turbulence intensity peak in figure 3(*b*) is partially an apparent one, i.e. part of the increase is a consequence of scaling the intensity with a velocity U_m which is not representative of the momentum flux in the entire cross-section. Most of the previous experimental studies were limited to the region $\xi' \leqslant 5$. In this region the turbulence intensity apparently rises to a maximum of 0.3.

The present study suggests that the streamwise region of the jet, that is influenced

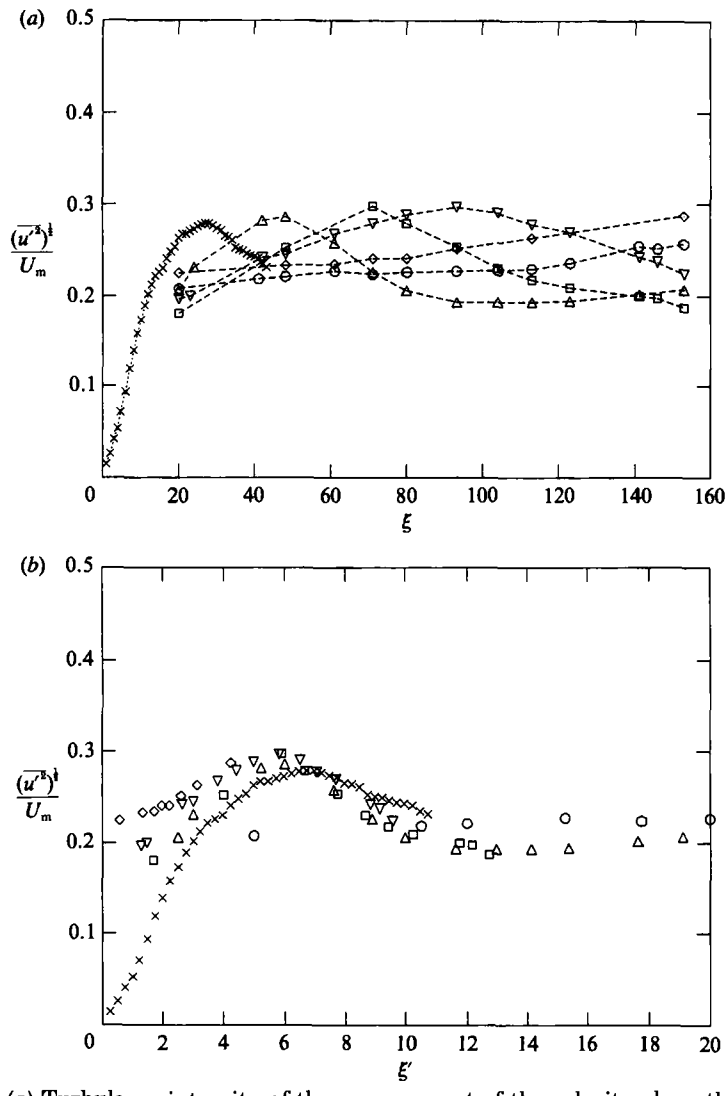

FIGURE 3. (*a*) Turbulence intensity of the u-component of the velocity along the axis of the jet as a function of $\xi = x/B$. (*b*) Same quantity presented as a function of $\xi' = x/H$. ○, $H/B = 4$; △, $H/B = 8$; □, $H/B = 12$; ▽, $H/B = 16$; ◇, $H/B = 36$; ×, Holdemann & Foss (1975), $H/B = 4$.

by secondary currents with rollers essentially oriented in the x-direction, scales with the depth H of the flow. The effect of the secondary currents is maximal at $\xi' \sim 6$ and becomes vanishingly small beyond $\xi' \sim 10$. As shown in figure 4 the extent of the zone influenced by secondary currents is of the same order for a solid and for a shear-free upper boundary.

The influence of the water depth on the development of the jet can also be seen in visual observations. Figure 5 shows six instantaneous pictures (exposure time $\frac{1}{60}$ s) of the dyed jet at water depths H/B between 2 and 36. All other experimental parameters were kept constant. The range of the jet depicted in all six pictures extends from $\xi = 0$ to $\xi = 300$ where $\xi = x/B$. For comparison, the distance $x = 10H$ is marked in each picture, except for the one from the experiment with depth $H/B = 36$, in which the visible segment of the jet is limited to $8H$.

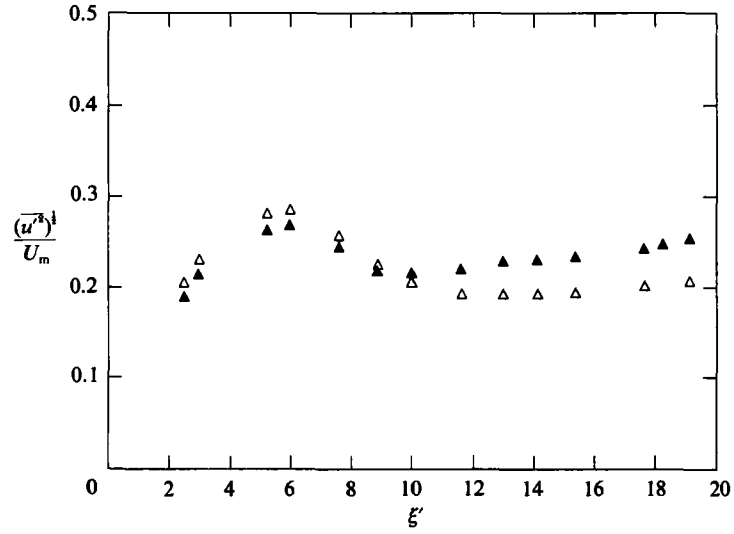

FIGURE 4. Turbulence intensity of the u-component along the axis of the jet, $H/B = 8$; △, no-slip upper boundary surface; ▲, shear-free upper bounding surface.

The photo in figure 5(*a*) was taken in an experiment with depth $H/B = 36$ and shows the typical behaviour of an unbounded two-dimensional jet with an approximately linear spread of the dye. Decreasing the depth of the water layer does not alter the situation described above within the region $\xi' < 10$ (see figures 5(*b*) and 5(*c*), in particular). Approximately at the point which corresponds to a local aspect ratio $b/H \simeq 1$, a slight undulation of the entire jet first appears. This perturbation grows rapidly and coherently over the full depth. At about $\xi' \simeq 15$–20 a mature 'meandering jet' form has developed. Within the range of our observations, the meandering motion seems to be preserved for yet larger distances. The only exception is found at the farthest distances for $H/B = 2$ (figure 5*f*), i.e. $\xi' \gtrsim 120$, at which some breakdown of the meandering motion seems to occur. This must be seen as the upper limit of validity for all the following considerations. The meandering jet is connected to a series of large two-dimensional vortical structures with an alternating sense of rotation which grow at the same rate as the overall growth of the jet. The structure of the flow is discussed later.

By installing a top glass plate rather than maintaining a free surface, the dynamic effect of a second bounding wall appears to have little effect on the generation and growth of the meandering motion. The apparent onset of the meandering begins in both cases at $\xi' \approx 10$.

Thus, using the water depth as the appropriate scaling parameter, a subdivision of the shallow plane jet into a near, a middle and far field is proposed.

The *near field* extends from $\xi' = 0$ to $\xi' \approx 2$. The flow behaves like a classical two-dimensional jet, where no significant influence of boundaries is felt in the jet proper. Measurements performed in the midplane are consequently representative for the bulk properties of the jet. Provided the slot width B is smaller than about $\frac{1}{8}H$, the near field can be subdivided in the usual way into a core zone, a transition zone and a zone with a fully developed flow.

The *middle field* extends from $\xi' \approx 2$ to $\xi' \approx 10$. The secondary currents which occur in the middle field affect the jet flow over the whole depth. Measurements which are performed in the midplane are no longer representative for the jet bulk properties.

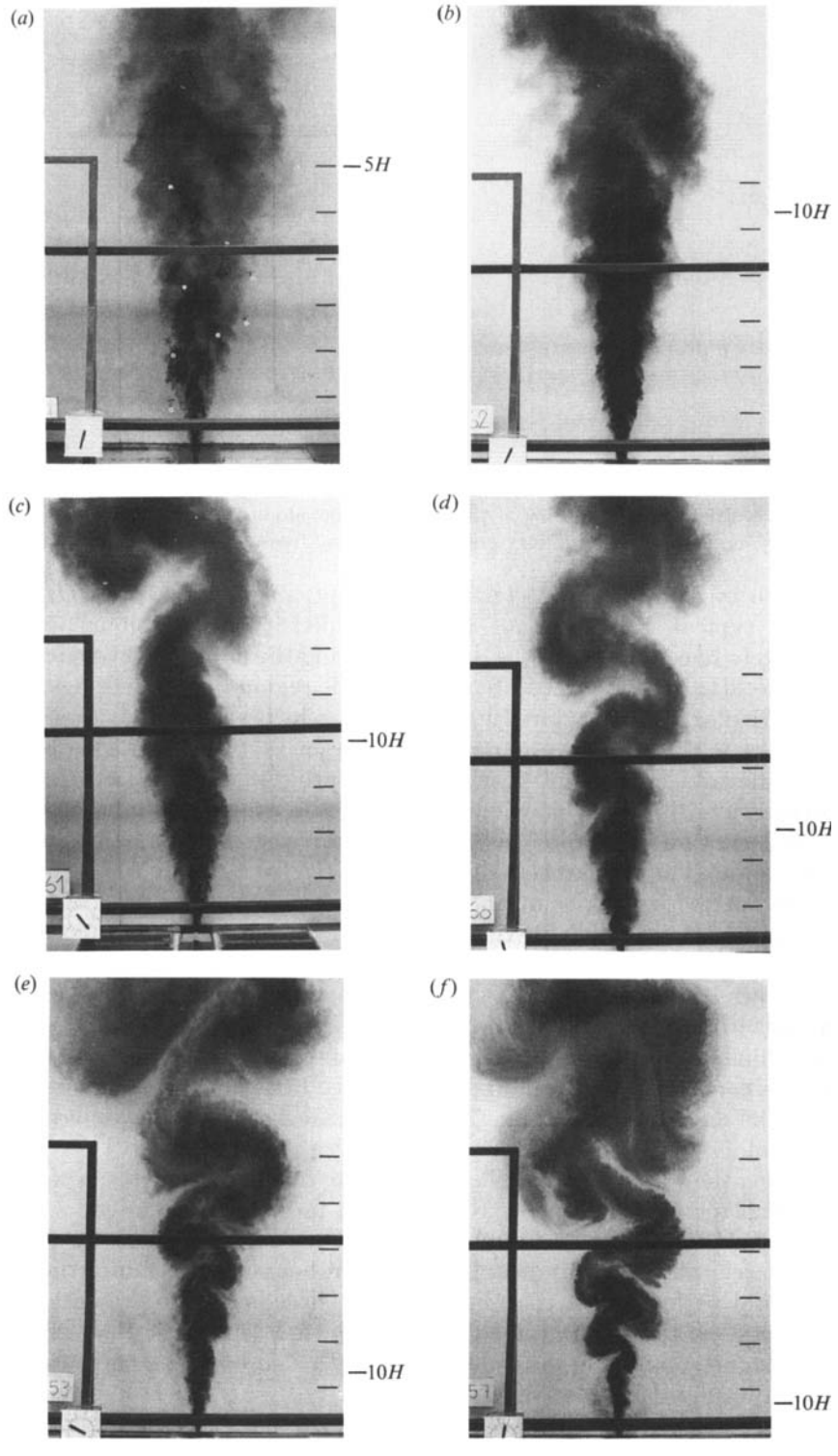

FIGURE 5. Instantaneous photographs of the jet (exposure time $\frac{1}{60}$ s) for: (*a*) $H/B = 36$, (*b*) $H/B = 16$, (*c*) $H/B = 12$, (*d*) $H/B = 8$, (*e*) $H/B = 4$, (*f*) $H/B = 2$. Solid bars are the support structure for the LDA system. Spacing between tick marks equals 30 cm or 30*B*.

The term *far field* refers to distances greater than about 10 times the depth H. The most conspicuous feature of the far field is the meandering motion of the jet in combination with the appearance of large counter-rotating vortices alternating on both sides of the vertical plane of symmetry of the jet.

According to the observations made in this study the mean velocity distribution in the jet cross-section in the near field is uniform in the z-direction, and the influence of the boundaries is limited to a thin layer close to these boundaries. In the middle field the velocity distribution in the z-direction is strongly non-uniform. Velocity maxima occur near the bounding surfaces. The far field is dominated by counter-rotating vortices, but the distribution of the mean velocity becomes again approximately uniform in the z-direction with only weak boundary influence. The location of the boundaries between near and middle field and middle and far field vary from one experiment to another. However, deviations from the values given above are found to be generally small.

4. Mean flow properties

Measurements of the u- and v-velocity component were conducted over a streamwise distance, $\xi = 20$ to $\xi = 153$ where $\xi = x/B$. Most of the measurements were performed using the set-up with the top glass plate in place. For the experiments with a free surface, a small glass plate of 40 mm diameter was installed in the light path in order to eliminate refraction problems due to the slightly wavy water surface. This plate was not immersed, but touched the water surface so that disturbances could be kept minimal. Measurements were made at selected points in the cross-sectional plane at a given x, with the majority of measuring points on the midplane. Only a few selected mean flow properties are presented here (more details are given by Giger 1987). Unless especially mentioned, all data shown represent the midplane.

Figure 6(*a*) shows transverse distributions of the mean forward velocity U. The centreline velocity U_m and the velocity half-width b were chosen as local scaling parameters. The measurements presented in figure 6(*a*) cover the range from the near field to the end of the part of the far field in which measurements were taken, i.e. $\xi' = 0.56$–38.25. Although significant differences exist in the structure of the flow, the measurements suggest a self-similar velocity distribution all over the near, middle and far field, which can be approximated by Reichardt's solution

$$U/U_m = \exp(-A\eta^2), \tag{1}$$

where $\eta = y/b$ is the dimensionless transverse coordinate. The numerical value for the constant is $A = -\ln(0.5) = 0.693$. Most of the other measurements known were conducted in the near field and show the same velocity distribution. The mean transverse velocity V for part of the data presented in figure 6(*a*) is shown in figure 6(*b*). The distribution is approximately the same in the near and the far field. For comparison, the distribution of V,

$$\frac{V}{U_m} = C_b\left\{-\frac{1}{2}\int_0^\eta \exp(-A\eta^2)\,d\eta + \eta\exp(-A\eta^2)\right\}, \tag{2}$$

computed from the two-dimensional continuity equations is drawn as a solid line in figure 6(*b*).

Strong deviations from the expected values occur in the middle field. Figure 7 shows two transverse profiles of the V-velocity components at $\xi' = 6$ for $H/B = 8$.

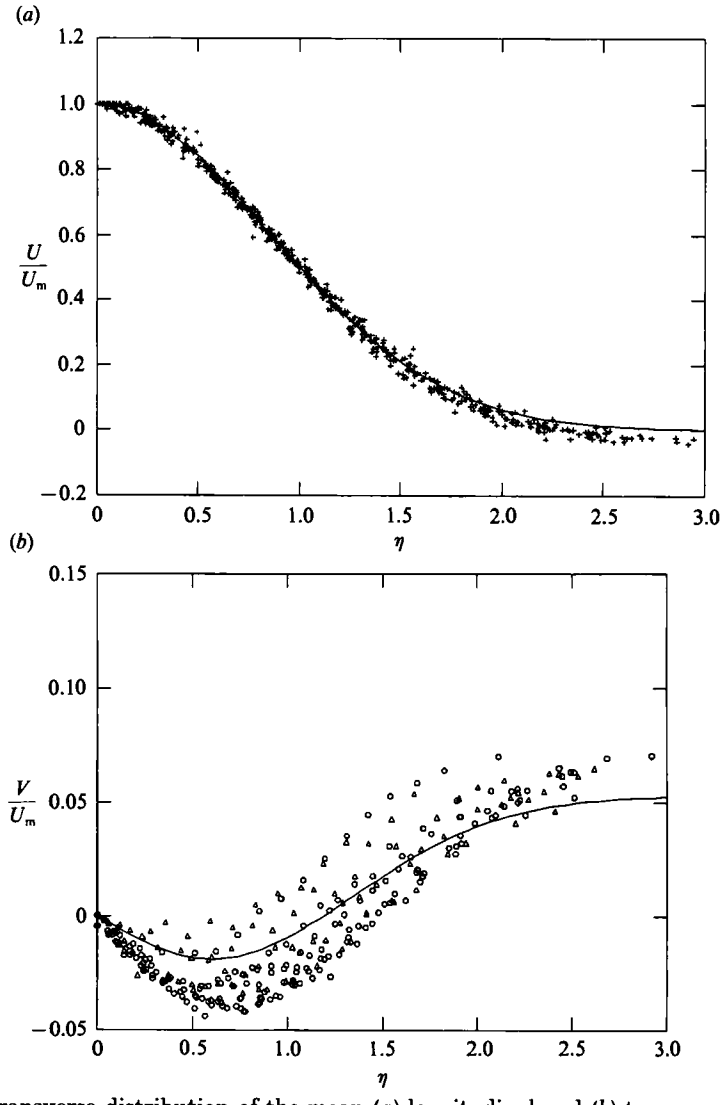

FIGURE 6. Transverse distribution of the mean (*a*) longitudinal and (*b*) transverse components of velocity, in the midplane of the jet, scaled by the mean centreline velocity U_m. The solid line in (*a*) represents equation (1), the solid line in (*b*) represents equation (2).

One of the profiles was measured in the midplane, $z/H = 0$, the other in a plane located at $z/H = -0.3$ below the midplane. While in the midplane V is everywhere negative, and thus directed inwards, i.e. towards the centreplane, the V velocity below the midplane is positive in a range $0 < \eta < 3.0$. At this level the direction of the flow is outwards. In the midplane the secondary currents transport slow ambient fluid towards the centreplane of the jet. The U component is consequently reduced. Near the confining boundaries fast fluid is transported from the centreplane outwards and the U component increases. This result is in agreement with the results of Foss & Jones (1968) shown in figure 6 of their publication. Figure 8 shows three long-exposure photographs of the same jet. The dye was injected near the bottom in the first, in the midplane in the second, and near the free surface in the third picture. The enhanced spreading both near the bottom and near the free surface suggests

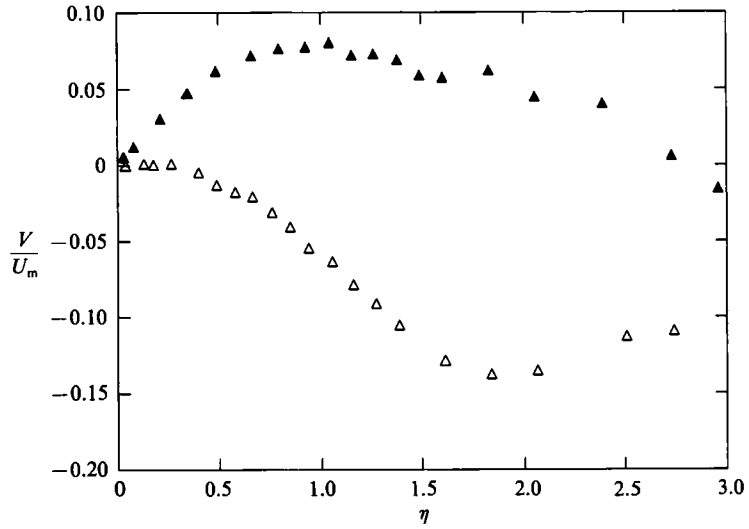

FIGURE 7. Transverse distribution of V/U_m at $\xi' = 6$. △, $Z/H = 0$; ▲, $Z/H = -0.3$. The V-component is negative in the midplane pointing towards the centreplane of the jet and positive in the range $\eta \leqslant 2.8$ in the plane $Z/H = -0.3$ pointing away from the centreplane of the jet.

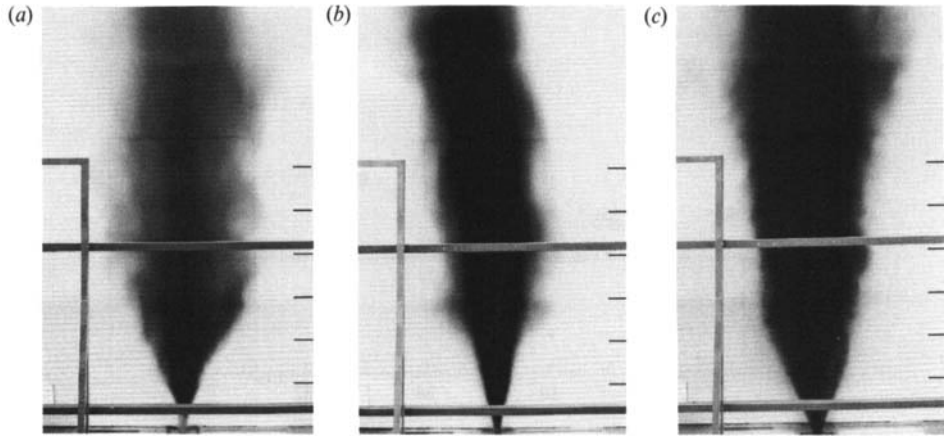

FIGURE 8. Long-exposure photographs (25 s) of flow visualization in an experiment with $H/B = 36$. (*a*) dye injected near the bottom, $z = -\frac{1}{2}H$; (*b*) dye injected in the midplane, $z = 0$; (*c*) dye injected near the free surface, $z = \frac{1}{2}H$.

that the secondary motions are induced primarily by the kinematic effect of any boundary and to a lesser extent by the nature of the boundary, i.e. whether it is solid or free.

The effect of the secondary flow on the mean velocity in the midplane is evident in figure 9. Figure 9(*a*) shows a distribution of the velocity ratio $(U_0/U_m)^2$ along the jet axis for experiments with different depths H/B. In the absence of secondary motion, i.e. for a truly self-similar jet, the velocity ratio would follow a straight line

$$(U_0/U_{mr})^2 = C_u(\xi - \xi_u) = C_u(H/B)(\xi' - \xi'_u). \tag{3}$$

Owing to the secondary currents developing in the middle field, the velocity U_m is smaller than the nominal centreline velocity U_{mr} given by the straight line (equation (3)). In this equation, ξ_u and ξ'_u, respectively, indicate the position of a kinematic

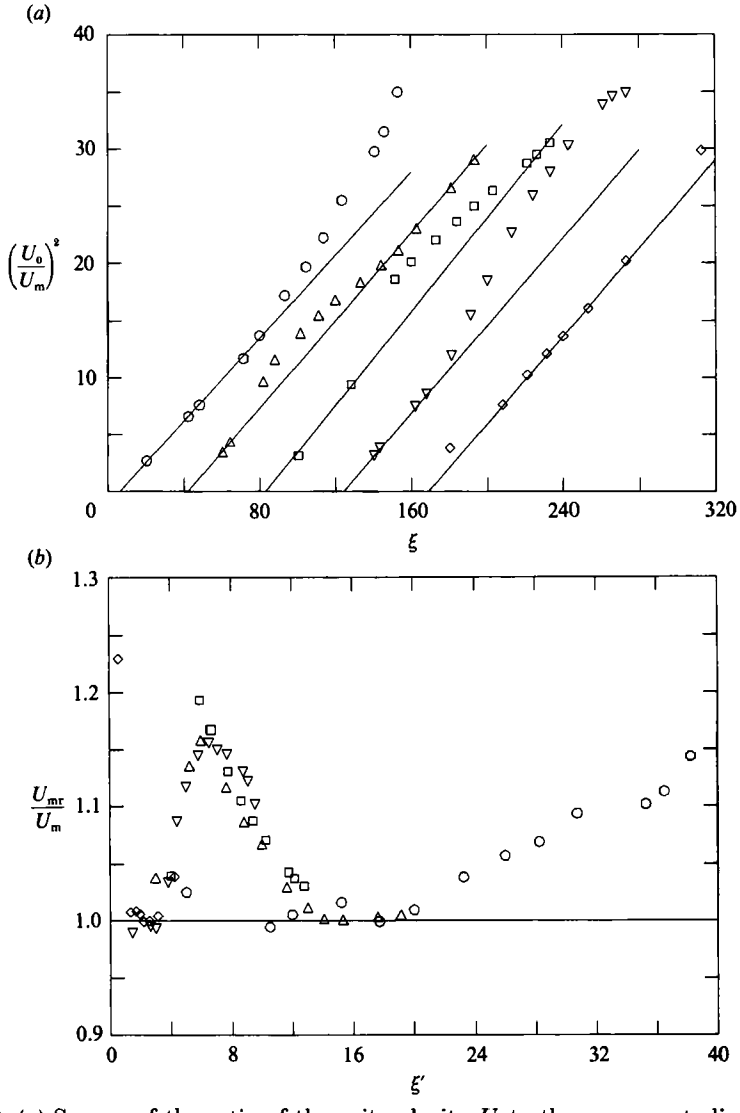

FIGURE 9. (*a*) Square of the ratio of the exit velocity U_0 to the mean centreline velocity U_m as a function of ξ. The abscissa origin for each experiment is successively shifted by 40 units. Straight lines represent the nominal velocity U_{mr}, equation (3). (*b*) Ratio of nominal mean centreline velocity U_{mr}, equation (2) to the measured centreline velocity U_m as a function of ξ'. The influence of the secondary currents is apparent in the range $2 < \xi' < 10$. Symbols as in figure 3.

H/B	C_u	ξ_u	ξ'_u	C_b	ξ_b	ξ'_b
4	0.182	6	1.50	0.100	6	1.50
8	0.192	2	0.25	0.100	0	0
12	0.205	3	0.25	0.106	3	0.25
16	0.192	4	0.25	0.100	0	0
36	0.192	9	0.25	0.095	0	0

TABLE 1

virtual origin. The values of C'_u, ξ_u and ξ'_u for experiments with different depths H/B are listed in table 1.

The region in which deviations of the centreline velocity U_m from its nominal value U_{mr} occur is associated with the secondary currents and thus scales with ξ' (figure 9*b*). It appears between $\xi' \approx 2$ and $\xi' \approx 10$. The experiment with $H/B = 4$ does not show any deviation of the centreline velocity from its nominal value in the middle field and the kinematic virtual origin is located at a greater distance from the orifice than in the other experiments. In the same experiment the centreline velocity in the far field becomes smaller than the nominal velocity given by (3), owing to the influence of skin friction at the no-slip bounding surfaces (Giger *et al.* 1991).

All jet quantities derived from the velocity U_m (the volume or momentum flux, for instance) show a behaviour similar to that illustrated in figure 9(*b*). The respective distributions are not shown here (see Giger 1987). Figure 3(*b*) shows that the streamwise turbulence intensity relative to U_m increases to reach a maximum of nearly 0.3 at approximately $\xi' = 6$. Beyond that point the streamwise turbulent intensity decreases and levels out to a value of approximately 0.22. In this regard, figure 9(*b*) suggests that the change of turbulence intensity, which in the range $2 < \xi' < 10$ increases by more than 30%, cannot be completely explained by the decrease of U_m by $\sim 15\%$, owing to the secondary currents developing in this range. Secondary currents thus cause a net increase of the r.m.s. values of u' and v' in the midplane. In the experiment with $H/B = 4$, secondary currents do not develop and the turbulence intensity $(u'^2)^{\frac{1}{2}}/U_{mr}$ has a constant value of approximately 2.20 over the entire range of ξ'.

The development of the r.m.s. values of u' and v' are further analysed with the help of figure 10. In figure 10(*a*), $(u'^2)^{\frac{1}{2}}/U_0$ is plotted logarithmically against ξ'. Measurements from the experiment with maximum depth, e.g. $H/B = 36$, are omitted as they do not extend beyond $\xi' = 5$. Self-similarity of the turbulence intensity demands that the data should align along straight lines with $-\frac{1}{2}$ slope. This is the case, except for an initial range of flow establishment and for the region from about $\xi' \approx 6$ to $\xi' \approx 10$. In this region the slope is nearly -1. On the other hand, in the experiment with depth $H/B = 4$, in which secondary flows do not develop, the slope is constant, equal to $-\frac{1}{2}$ for $\xi' > 5$.

A similar behaviour is observed in the plot of $(v'^2)^{\frac{1}{2}}/U_0$ as a function of ξ' (figure 10*b*). However, in this case the slope of the straight lines is $-\frac{1}{4}$ and $-\frac{3}{4}$, respectively.

In the range $0 \leqslant \xi' \leqslant 5$, the ratio $(v'^2)^{\frac{1}{2}}/(u'^2)^{\frac{1}{2}}$ is constant, close to unity. For $\xi' \geqslant 5$, on the contrary, the ratio $(v'^2)^{\frac{1}{2}}/(u'^2)^{\frac{1}{2}}$ increases proportionally to $\xi'^{\frac{1}{4}}$. Note that, as shown in figure 3(*b*), beyond the region influenced by the secondary current, i.e. $\xi' \gtrsim 10$, the intensity $(u'^2)^{\frac{1}{2}}/U_{mr}$ becomes constant. The intensity $(v'^2)^{\frac{1}{2}}/U_{mr}$, by contrast, continuously increases in the same region.

In the range $\xi' < 5$ an isotropy of the turbulent fluctuations in the u- and v-directions is observed in the midplane. This is not necessarily the case for the w-component. In fact, it is the anisotropy of the turbulent fluctuations in the v- and w-directions occurring between the midplane and centreplane and especially between the latter and the bounding surfaces which are the cause for the secondary currents (Perkins 1970).

The results presented suggest that the zone of flow establishment scales with B and that it can extend up to $40B$. In the experiment with $H/B = 4$, $x/B = 40$ corresponds to $\xi' = 10$. The relatively large positive shift of the geometric and kinematic virtual origins, e.g. $\xi'_b = \xi'_u = 1.5$, and a long region of the flow establishment may be the reason why secondary currents did not develop in this experiment.

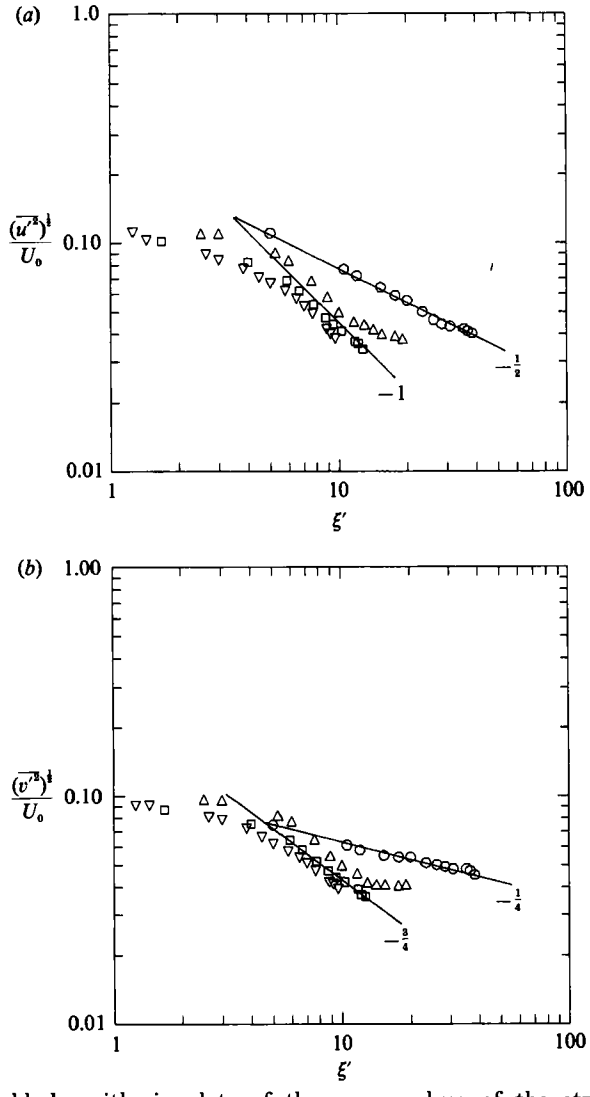

FIGURE 10. Double-logarithmic plots of the r.m.s.-values of the streamwise and transverse velocities fluctuations scaled with U_0 as a function of ξ'. (*a*) $(\overline{u'^2})^{\frac{1}{2}}/U_0$, (*b*) $(\overline{v'^2})^{\frac{1}{2}}/U_0$. Symbols as in figure 3.

The growth of the jet half-width measured in the midplane in experiments with different depths is shown in figure 11. The nominal half-width b_r of a self similar jet grows linearly with x:

$$b_r/B = C_b(\xi - \xi_b), \tag{4}$$

or

$$b_r/H = C_b(\xi' - \xi'_b). \tag{5}$$

Relative to this nominal behaviour the data show again slight deviations in the middle field. The values of c_b and ξ_b, ξ'_b respectively, are listed in table 1. The minimal half-width is about 94% of its nominal value, followed by an overshoot up to 106%. Beyond $\xi' \approx 10$, linear spreading is again approached. In the experiment with depth $H/B = 4$ no deviations from the nominal width b_r occur over the whole range of observation.

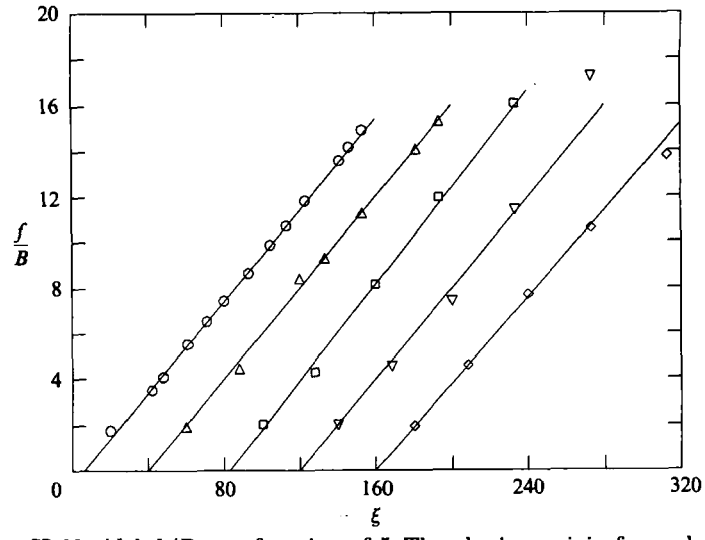

FIGURE 11. Half-width b/B as a function of ξ. The abscissa origin for each experiment is successively shifted by 40 units. Symbols as in figure 3.

5. The structure of the jet in the far field

The structure of the jet in the far field is elucidated with the help of figure 12, which shows a series of 6 short exposure photographs taken in an experiment with $H/B = 4$. In addition to the dye added to the jet discharge, confetti was strewn on the water surface. The paths of the confetti during the exposure time of 1 s appear as bright lines on these photographs. These streaklines are short enough to give as an ensemble a representative picture of the instantaneous flow field. The most striking features in this visualization of the jet flow are a series of large-scale two-dimensional vortical structures. These vortices align along two rows, one on each side of the axis of the jet. The vortices in each row have the same direction of rotation and are counter-rotating and mostly staggered, relative to the other row. Between these two rows of vortices, jet fluid meanders at relatively high velocity. At the beginning of the far field, that is to say at $\xi' \approx 10$, where oscillations of the jet are visually observed for the first time, the half-width b of the jet is nearly equal to the depth H. The visual observations presented in figure 5, in which sharp interfaces between dyed jet fluid and non-dyed ambient fluid extending from the bottom to the surface are visible, suggest that these structures are predominantly two-dimensional except in the vicinity of the bottom where the no-slip condition influences the flow. As will be shown below in the far-field the flow in the jet is strongly determined by these vortices and their interactions.

A number of photographs taken at short-time intervals in an experiment with depth $H/B = 4$ enable the number of vortices passing a number of stations located at different distances x/B to be counted. The resulting frequency f_v is given in figure 13. Its dependence on x/B is given by the solid line in this figure, which corresponds to the relation

$$f_v = 176\,(\xi)^{-\frac{3}{2}}. \tag{6}$$

f_v thus fulfils the similarity requirements and can be scaled by local parameters like b_r and U_{mr} to give a constant Strouhal number $St_v = f_v . b_r/U_{mr} = 0.07$.

The decrease of the frequency f_v is caused by the decrease of the transport velocity of the vortical structures and by the reduction of their number by pairing. The latter

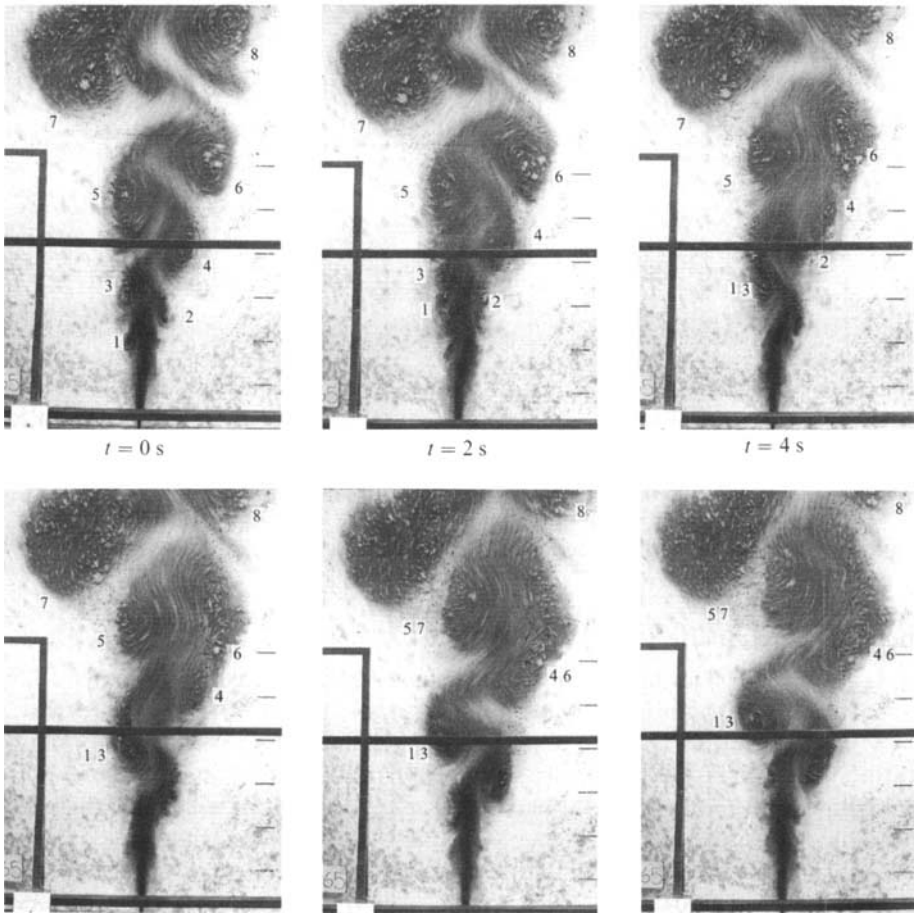

FIGURE 12. Sequence of 6 photographs of the dyed jet with confetti added at the water surface, $H/B = 4$. Exposures are 2 s apart. Pairing of vortical structures: At $t = 4$ s vortices 1 and 3 have paired, at $t = 8$ s vortices 4 and 6 as well as 5 and 7 have paired.

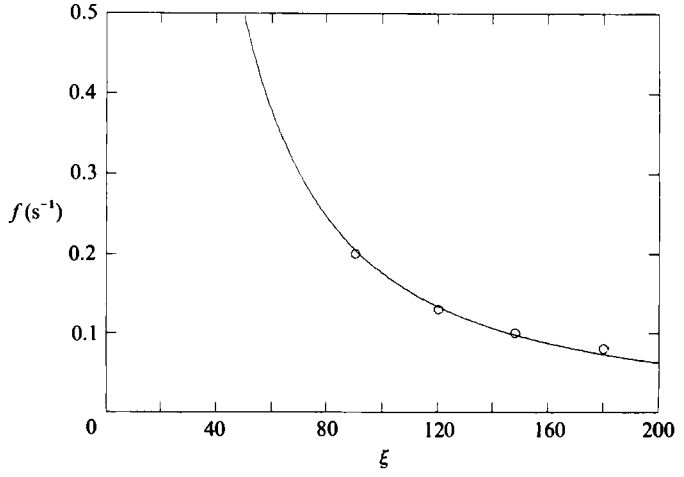

FIGURE 13. Passing frequency of 'vortical structures' as observed in figure 12 determined from a large number of photographs as a function of ξ. Solid line: equation (7).

can be observed in the photographs presented in figure 12. The timestep between these photographs is 2 s. The 'vortices' observed in the first exposure are labelled 1–8. In the second exposure ($t = 2$ s) vortices 1 and 3 approach each other. Another 2 s later (exposure 3) these two vortices merge to one designated by 1, 3. In the fourth exposure ($t = 6$ s) vortices 4 and 6 as well as 5 and 7 approach each other. The pairing of vortices 4 and 6 on the left-hand side of the picture, and vortices 5 and 7 on the right-hand side of the picture is completed in the following two exposures ($t = 8$ and $t = 10$ s).

The course of a vortex pairing observed in the present flow visualizations differs from the one observed in shear layers at low Reynolds numbers. This can be illustrated by following the pattern of pairing of vortices 4 and 6 shown in figure 12. In the timestep elapsed between $t = 2.0$ s and $t = 4.0$ s the two vortices have approached each other. At the same time vortex 6 has taken on an elongated form. Two seconds later the pairing is already completed. In the following 2 s the new vortex 4, 6 changes only its form and exhibits a smaller aspect ratio. The same pattern is observed in the pairing of vortices 1 and 3 as well as 5 and 7, and is typical for the pairing of vortices in all experiments. The merging of the vortices occurs without previous rotation of the two vortices around a common axis as described by Winant & Browand (1974), Cantwell (1981) or Hussain (1986), for example. The picture observed in the present study resembles the process of tearing proposed by Moore & Saffman (1975), later observed by Dimotakis & Brown (1976) in a turbulent mixing layer at large Reynolds number.

6. Development of quasi-two-dimensional turbulence in the far field

The visual observations and, in particular, the two-dimensionality of the vortical structures are confirmed by the energy spectra computed from the time records of the velocity. Figure 14 shows some typical one-dimensional energy spectra of the turbulent fluctuations u', v' of the longitudinal and transverse velocity components. The spectra are presented in non-dimensional form. Scaling parameters are in all cases the nominal centreline velocity U_{mr} determined from (3), and the nominal half-width b_{r} determined from (4). The spectra in figures 14(*a*) and 14(*c*) are computed from measurements taken in an experiment with flow depth $H/B = 16$ at a distance of $\xi' = 2.6$, 5.0 and 9.6, respectively. The first of these points of measurement is located near the beginning, the second near the centre, and the last near the end of the middle field. There is a distinct energy peak in the v'-spectra (figure 14*c*). Spectra measured in the near field of plane jets by other authors (Goldschmidt & Young 1975) are similar to the ones presented in figures 14(*a*) and 14(*c*). A universal equilibrium range and an unequivocally distinguishable inertial subrange with a $-\frac{5}{3}$ wavenumber dependence, typical for a three-dimensional cascading turbulent flow, are observed at higher Strouhal numbers. The structure of turbulence and, in particular, its three-dimensional character are not significantly influenced by the secondary currents present in the middle field of the jet.

Power spectra in the far field (figures 14*b* and 14*d*) behave quite differently. The spectra in figures 14(*b*) and 14(*d*) are from an experiment with flow depth $H/B = 4$. The velocity measurements were taken at $\xi' = 10.50$, 20.00 and 38.25. The first of these loci is situated near the beginning of the far field. In the middle field the non-dimensional maxima of the energy density of the spectra are nearly constant, suggesting an increase of the maximum energy density proportional to $\xi'^{\frac{1}{2}}$ in accordance with the similarity requirements. In the far field the maxima of the non-

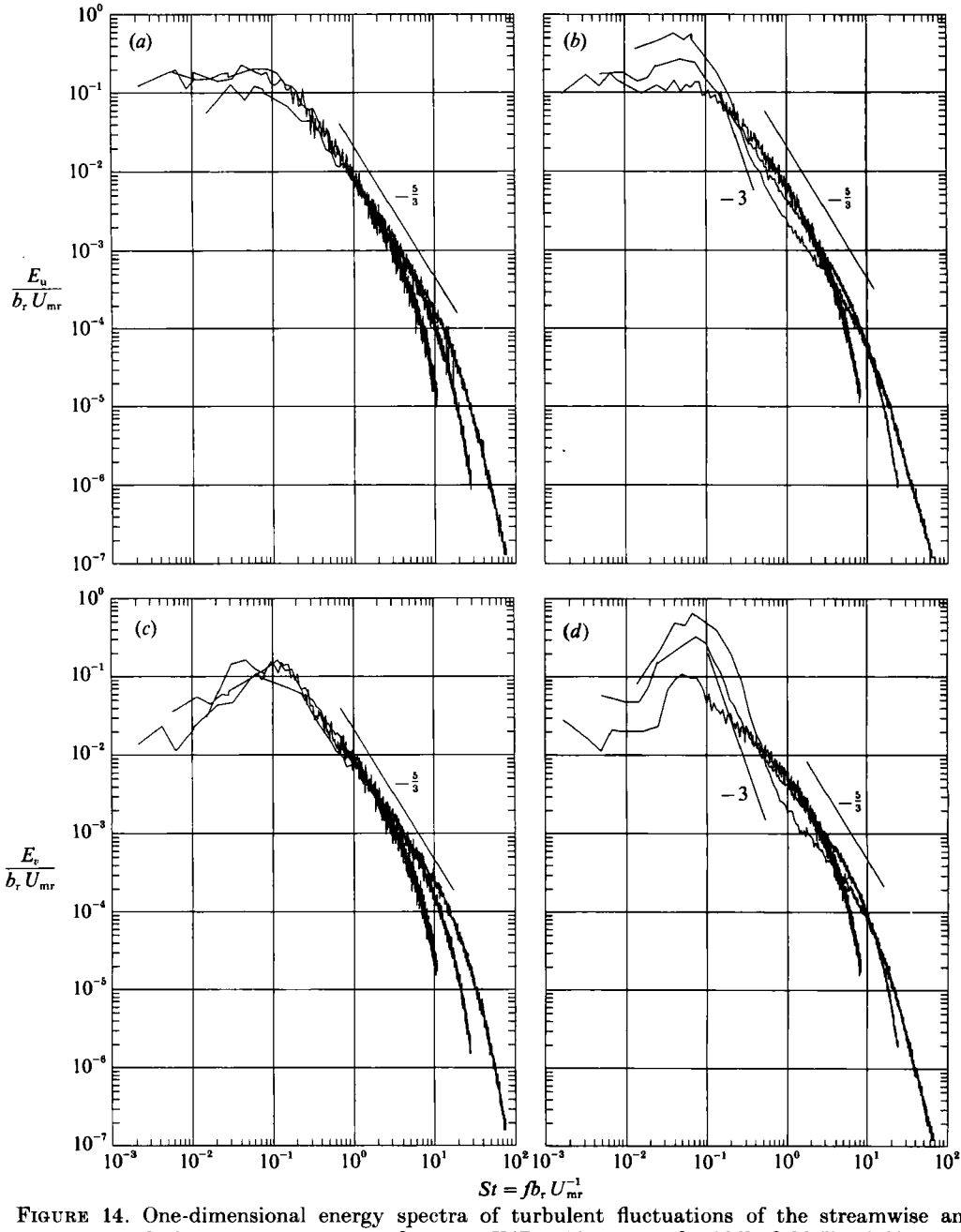

FIGURE 14. One-dimensional energy spectra of turbulent fluctuations of the streamwise and transverse velocity components. (*a*) u-Spectra: $H/B = 16$, near and middle field $\xi' = 2.625$, 5.00, 9.5625. (*b*) u-Spectra: $H/B = 4$, far field $\xi' = 10.50$, 20.00, 38.25. (*c*) v-Spectra: for same conditions as (*a*). (*d*) v-Spectra: for same conditions as (*b*).

dimensional energy density increase significantly faster with ξ'. At the same time, the peak around the maximum becomes more pronounced. In addition, a range develops in which the energy transfer follows a -3 wavenumber dependence. Such a wavenumber dependence is consistent with the development of quasi-two-dimensional turbulence characterized by an enstrophy cascade (Batchelor 1969). The

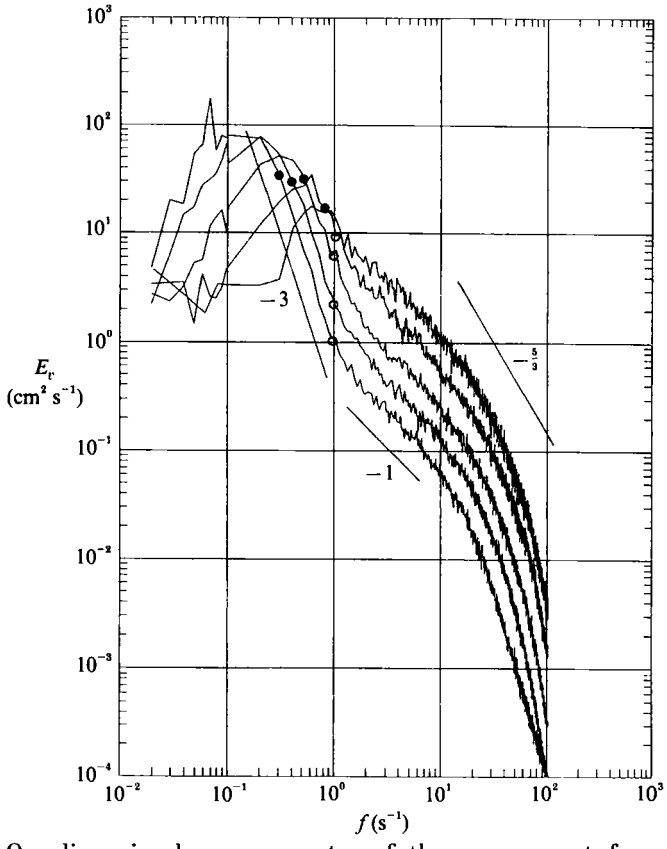

FIGURE 15. One-dimensional energy spectra of the v-component from an experiment with $H/B = 4$. From right to left: $\xi' = 10.50$, $\xi' = 15.25$, $\xi' = 23.25$, $\xi' = 30.75$, $\xi' = 38.25$. Solid circles represent the beginning and open circles the end of the -3 range of the spectra.

alleviation of the energy cascade in the quasi-two-dimensional part of the spectrum causes a depletion of the energy content in higher wavenumbers. At even larger wavenumbers the energy transfer gradually relaxes back to that for three-dimensional turbulence. This relaxation range seems to follow a -1 wavenumber dependence (see also figure 15).

The shapes of the spectra suggest that the energy extracted from the inertial subrange of the spectrum is injected at the location at which the enstrophy cascade begins and is transferred in an inverse energy cascade towards the peak, which increases in magnitude.

The instability of plane laminar jets has been investigated by different authors (Sato 1960; Michalke & Schade 1963; Ikeda 1977). Cervantes (1981) remarks that the instability of turbulent jets can be treated in a similar way. Small-scale turbulence can be taken into account if an appropriate eddy-viscosity concept is adopted and mainly influences the growth of the amplitude of the most amplified mode. Here only an estimate of the most amplified mode is sought. Thus, following the analysis by Michalke & Schade (1963), the transverse velocity profile can be approximated by a trapezoidal distribution with $U/U_m = 1$ for $y/b < 0.2$ and $U/U_m = 1-(y/b-0.2)/1.5$ for $0.2 < y/b < 1.7$. The form factor, i.e. the slope of the profile, is $\delta = 0.67$. It follows that the wavenumber of the most amplified disturbance is $\alpha \approx 0.75\ (1.5b)^{-1}$, and the corresponding wavelength is $\lambda \simeq 2.0b$. From numerical simulations it is known that

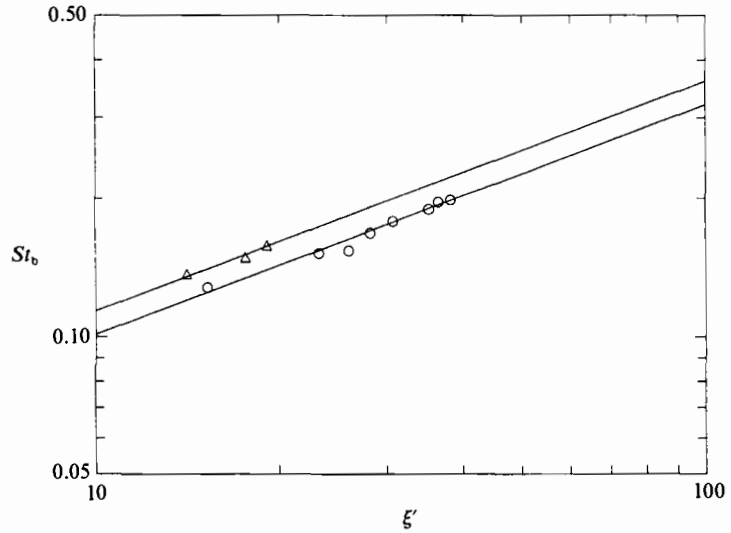

FIGURE 16. Double-logarithmic plot of the change of the Strouhal-number at the beginning St_b of the -3 slope range of the spectra as a function of ξ'. ○, $H/B = 4$; △, $H/B = 8$.

the size of the vortical structures is approximately equal to $\frac{1}{2}\lambda$, or in this case, equal to b. This estimate is in good agreement with the size of the vortices observed visually in the present experiments. These considerations are based on the mean flow profile of the jet, which is inherently unstable. Vortical structures due to instability can thus form at any distance ξ' from the orifice.

At distances of $(\xi' - \xi'_b) = 10$ the halfwidth b of the jet is equal to the depth H. Beyond $(\xi - \xi'_b) \approx 10$ the size of such structures becomes larger than H and they can only exist if their axis is and remains perpendicular to the midplane. Such vortical structures have parallel axes and the same sense of rotation and thus increase in size by pairing. This kinematic constraint seems to be the cause for the development of the observed vortical structures at distances larger than $10H$ from the geometric virtual origin of the jet and consequently of the appearance of a quasi-two-dimensional range in the energy spectra in the far field.

To study the development of the two-dimensional range of the spectra with distance ξ' a number of energy spectra of the v-component were computed in the range $10 < \xi' < 40$ with the use of data from experiments with depth $H/B = 4$ and 8. Part of the v-spectra is presented in non-scaled form in figure 15. The beginning and end of the -3 slope range, as well as the corresponding frequencies f_b and f_e, were determined in each spectrum. For this purpose the following procedure was used: The start frequency f_b was determined as the intersection of a constant plateau line and a -3 slope line fitted to each spectrum. In a similar way, the end frequency f_e was found as the intersection of a -3 slope line and a -1 slope line. These points are shown in figure 15 as solid circles for f_b and as empty circles for f_e, respectively. The resulting Strouhal numbers St_b and St_e were then computed as mentioned earlier by using the local nominal centreline velocity U_{mr} and the nominal width b_r as scaling parameters. As shown in figure 16, the Strouhal number St_b increases proportionally to $\xi'^{\frac{1}{3}}$. This corresponds to a decrease of the wavenumber k_b proportionally to $\xi'^{-\frac{1}{3}}$. The proportionality constants are 0.032 for experiments with depth $H/B = 4$ and 0.036 for experiments with depth $H/B = 8$.

The frequency f_e, corresponding to the end of the -3 slope in the spectra, is

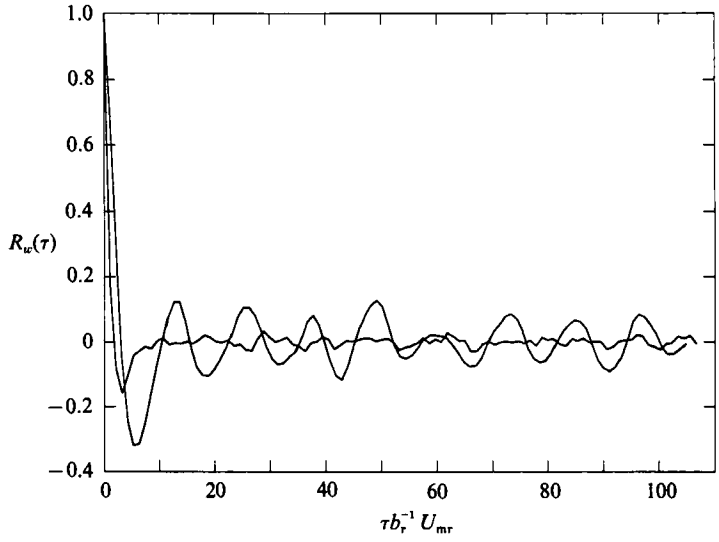

FIGURE 17. Autocorrelation function $R_{vv}(0,0,0,\tau)$. For $H/B = 16$, $\xi' = 2.625$, no oscillation; for $H/B = 4$, $\xi' = 38.25$, quasi-periodic oscillations.

independent of ξ' for experiments at a given depth, e.g. $f_e = 1\ s^{-1}$ for $H/B = 4$ and $f_e = 0.4\ s^{-1}$ for $H/B = 8$. This implies a $\xi'^{\frac{3}{2}}$ dependence of the Strouhal number St_e. The corresponding proportionality factors are 0.0028 and 0.0036, respectively.

The inverse of the Strouhal number can also be interpreted as a non-dimensional wavelength $\lambda^* = \lambda/b$ with $\lambda = U_{mr}/f$. The ratio $\lambda_b/\lambda_e = St_e/St_b$ increases linearly with ξ'. The location at which λ_b/λ_e becomes 1 indicates the beginning of the development of a -3 range in the spectra. This location is found to be $\xi' = 11.51$ for the experiment with $H/B = 4$ and $\xi' = 10$ for the one with $H/B = 8$. The difference in location is practically identical to the difference in the location of the geometric virtual origin for these two depths.

One can thus write:

$$St_b = C_1(\xi' - \xi'_b)^{\frac{1}{2}}, \tag{7}$$

$$St_e = C_2(\xi' - \xi'_b)^{\frac{3}{2}}, \tag{8}$$

valid for $(\xi' - \xi'_b) > 10$.

The numerical values $C_1 = 0.036$ and $C_2 = 0.0036$ were determined from the present experiments. Notice that for $\xi' - \xi'_b = 10$ these Strouhal numbers become $St_b = St_e = 0.11$, which is in good agreement with the Strouhal number of 0.1 determined by Michalke & Schade (1963) for the frequency of the most amplified disturbance.

The large-scale motions appearing in the far field give rise to quasi-periodic oscillations in the autocorrelation function R_{vv}, which do not appear in such functions in the near and middle field. Figure 17 shows the autocorrelation functions computed for measuring points on the axis of the jet at $\xi' = 2.625$, $H/B = 16$ and $\xi' = 38.25$, $H/B = 4$. The lag-time τ scaled with U_{mr} and b_r corresponds to the inverse of the Strouhal number appearing in the spectra.

From the zero crossings of the oscillating parts of the autocorrelation function one can estimate a mean period of oscillation and the associated Strouhal number, e.g. $St = 0.0824$. This Strouhal number is in excellent agreement with the Strouhal number St_p at the peak of the energy spectrum, which in this case is estimated to be $St_p \approx 0.085$ (see figure 14*d*), and is related to the quasi-periodic meandering motion of the jet in the far field.

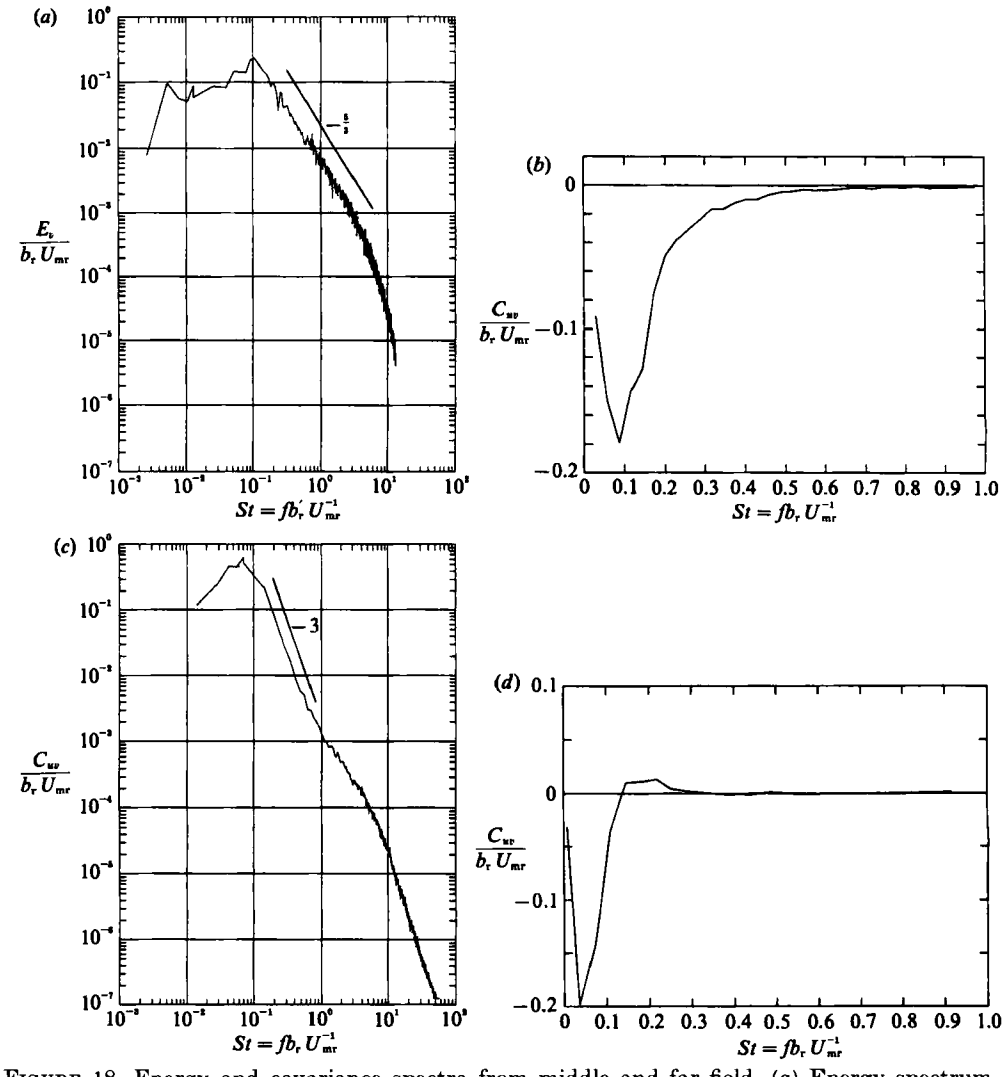

FIGURE 18. Energy and covariance spectra from middle and far field. (*a*) Energy spectrum, *v*-component, $H/B = 16$, $\xi' = 3.00$, (middle field) $\eta' = 0.7$. (*b*) Covariance spectrum at same location. (*c*) Energy spectrum, *v*-component, $H/B = 4$, $\xi' = 38.25$, (far field) $\eta' = 0.7$. (*d*) Covariance spectrum at same location.

The Eulerian integral lateral lengthscale Λ_e can be estimated by integration of the autocorrelation function up to the first zero crossing. If scaled by b, one gets $\Lambda_e/b \approx 0.727$ for $\xi = 2.625$ in the beginning of the middle field, and $\Lambda_{e,fb} = 1.567$ for $\xi' = 38.25$ in the far field. The value $\Lambda_e/b \approx 0.727$ is of the order of magnitude given by Goldschmidt & Bradshaw (1981). Owing to the formation and pairing of the large vortical structures in the far field this length becomes roughly twice as large.

Another important feature of the coherent vortical structures in the far field is the production of shear in the braids between the vortices. It is believed that most of the turbulent shear stems from these braids. For this purpose, the covariance spectrum was computed at point $\xi' = 3.0$, $\eta = 0.7$ in an experiment with depth $H/B = 16$ and at point $\xi' = 38.25$, $\eta = 0.7$ in an experiment with $H/B = 4$. At $\eta = 0.7$ the profile of the mean velocity has a maximum slope, and the turbulent shear stress attains its

maximum. The cospectra are shown in non-dimensional form in figures 18(*b*) and 18(*d*). For comparison, the power spectra of the lateral velocity fluctuations v' at the same locations are given in figures 18(*a*) and 18(*c*).

At $\xi' = 3$ the spectra correspond to spectra in the near field. At $\xi' = 38.25$ the quasi-two-dimensional turbulence is well developed. The power spectrum at this point, plotted in figure 18(*c*), has a range with a -3 slope extending approximately from the Strouhal number $St_b \approx 0.21$ to $St_e \approx 0.64$. A distinct peak appears at $St_p \approx 0.08$. The corresponding covariance spectrum is presented in figure 18(*d*). Unexpectedly, this spectrum has a positive part in the range $0.15 < St_{uv} < 0.375$ and its peak occurs at $St_{uv} \approx 0.041$, e.g. at about half the frequency of the peak in the power spectrum.

The frequency f_v, at which vortices pass the measurement location, is given by (6). The average frequency for the passage of a pair of vortices can be computed from

$$f_p = \frac{df_v}{dx}\lambda_v. \tag{9}$$

λ_v is the average distance in the x-direction between the centres of the vortices in a row. At the point at which the spectra were determined, $\lambda_v = 0.7$ m was found from the analysis of a large number of photos. Remembering that the Strouhal number is the inverse of a wavelength scaled by b_r, we get from (7) for $\xi' = 38.25$, $\lambda_b = 0.74$ m, which is in good agreement with the visual determination, and shows that this wavelength is a measure for the average spacing of the centre of the vortices in a row. The resulting pairing frequency St_{vp} is 0.042 or 0.044, respectively, which is in good agreement with $St_{uv} = 0.041$. The reduction of the peak frequency of the covariance spectrum to half of the frequency at which the energy peak occurs is thus related to vortex pairing. This conclusion is supported by the comparison with the covariance spectrum at $\xi' = 3$, $\eta = 0.7$, shown in figure 18(*b*). As expected, this spectrum has no positive part and peaks at $St_{uv} \approx 0.9$, i.e. at nearly the same location at which the power spectrum (figure 18*a*) has its maximum. If we assume, supported by these observations, that in the far field the frequencies in the cospectrum are reduced by a factor of 0.5, the positive part of the cospectrum in figure 18(*d*) is related to the extraction of energy in the quasi-two-dimensional range of the power spectrum presented in figure 18(*c*).

7. Intermittency

Intermittency is closely related to entrainment and mixing of ambient irrotational fluid (Townsend 1976). The signal of an LDA anemometer taken at a point close to the lateral boundary of the jet shows periods of turbulent flow with fluctuations in a broad frequency range and periods of non-turbulent flow. The latter show only low-frequency variations of the velocity induced by the large eddies mainly responsible for the entrainment of ambient non-turbulent fluid. The intermittency factor γ is defined as

$$\gamma = \lim_{T\to\infty} \frac{1}{T}\int_0^T I(t)\,dt. \tag{10}$$

$I(t)$ is an intermittency function with the value 1, where the signal is turbulent, and 0, where the signal is non-turbulent.

The procedure used to determine the intermittency function is similar to the one used by Heskestad (1965). The LDA signal is first low-pass filtered. This allows the decomposition of the LDA signal $U(t)$ in a low-frequency non-turbulent part $\tilde{u}(t)$ and

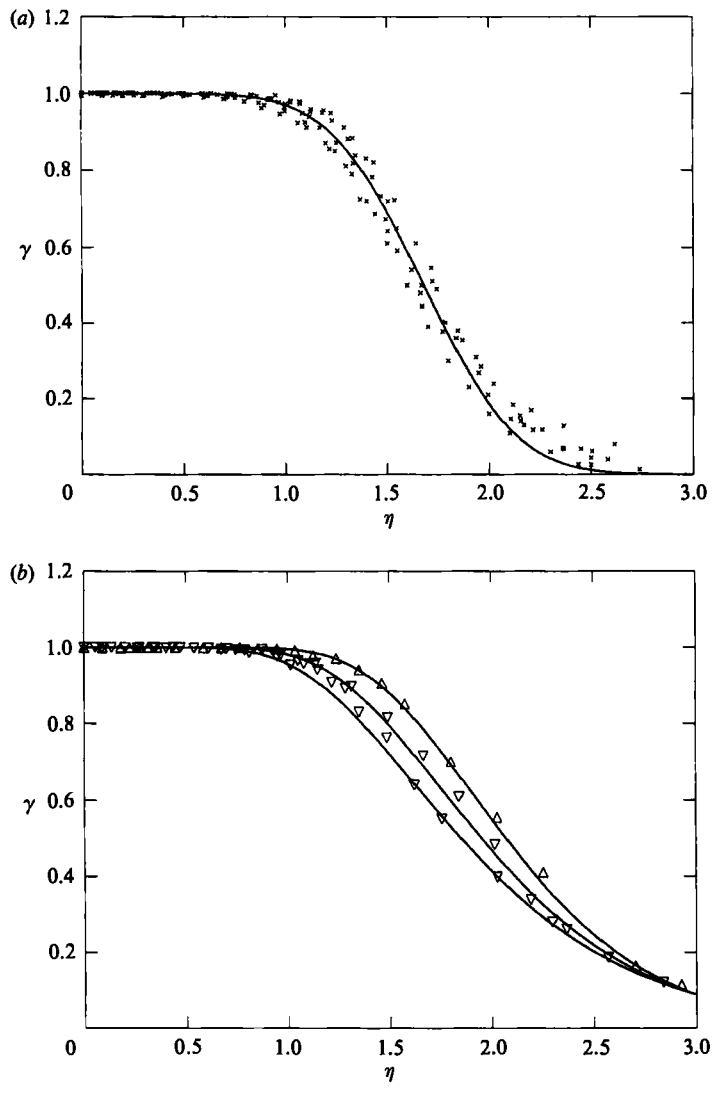

FIGURE 19. Intermittency factor distribution in transverse direction: (*a*) In the range $\xi' < 3$ and $9 < \xi' < 12$. Full-line: Gaussian distribution with $\gamma = 0.5$, at $\eta_{0.5} = 1.68$, $s_\gamma = 0.36$. (*b*) In the range $3 < \xi' < 9$ (middle field). Full lines: long-normal distributions.

a high-frequency 'turbulent' part $u''(t)$. The square of the latter is used as a detection function and its comparison with a threshold value u''^2_{th} allows the determination of the intermittency function. To eliminate the 'non-turbulent' spots artificially introduced at the zero crossings of the u'' function a minimum duration t_{sp} of the non-turbulent sequence is required. If the duration is shorter than t_{sp}, the sequence is considered to be part of the adjacent turbulent sequences, which are thus connected.

This procedure requires the determination of three parameters, the window width of the filter T_f, the threshold u''^2_{th} and the minimum duration t_{sp} of non-turbulent sequences. The first of these parameters was determined by inspection and the last two by a trial and error method. (For more details see Giger 1987.) For the data available in the present study this approach proved to be more reliable and effective than those based on the use of derivatives.

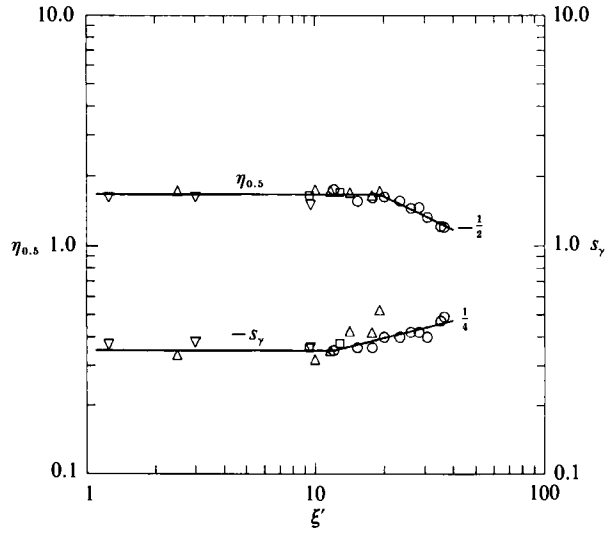

FIGURE 20. Double-logarithmic plot of the location $\eta_{0.5}$ of the $\gamma = 0.5$ point and standard deviation s_γ of the intermittency factor distribution as a function of ξ'. Symbols as in figure 3. Straight lines represent equations (12) and (13), respectively.

The transverse distribution of the intermittency factor in the near field is wider than the one of Davies, Keffer & Baines (1975), but in good agreement with that of Heskestad (1965) and Gutmark & Wygnanski (1976). Corrsin & Kistler (1954) predict that this distribution is nearly Gaussian and give the relation

$$\sigma(x)/b = [(\overline{v'^2})^{\frac{1}{2}}/U_m](2\Lambda_L \xi/b)^{\frac{1}{2}} \tag{11}$$

for its standard deviation, written here in non-dimensional form. Λ_L is the longitudinal Lagrangian lengthscale. If all parameters on the right-hand side are self-similar, $s_\gamma(\xi) = \sigma_\gamma(x)/b$ is a constant.

In the range $\xi' < 3$, i.e. the near field, and in the range $9 < \xi' < 12$ of the far field the distribution of γ is similar and nearly Gaussian. Intermittency distributions determined from eight measurements at three different depths H, covering these two ranges, are shown in figure 19(*a*). The full line in this figure is a Gaussian distribution with $\gamma = 0.5$ located at $\eta_{0.5} = 1.68$ and a standard deviation $s_\gamma = 0.36$. The deviations of the corresponding parameters of Gaussian distributions fitted to the individual results of the eight experiments from the values given above are small, e.g. ± 0.054 for $\eta_{0.5}$ and ± 0.022 for s_γ.

In fact, the location of the $\gamma = 0.5$ point does not change for ξ' up to about 20. For $\xi' > 20$ the distance $\eta_{0.5}$ of the $\gamma = 0.5$ point from the axis of the jet decreases proportionally to $\xi'^{-\frac{1}{2}}$ (figure 20). This decrease apparently starts when the vortical structures are completely developed. The standard deviation s_γ of the γ-distribution in transverse direction already starts increasing at $\xi' \approx 10$. As a result of the self-similarity of the velocity distribution in the far field both b an Λ_L are proportional to x in this region. In this case, $(\Lambda_L x/b^2)^{\frac{1}{2}}$ is constant and the change of s_γ depends, according to (11), only on the change of $(\overline{v'^2})^{\frac{1}{2}}/U_m$. In the far field, U_m is proportional to $x^{-\frac{1}{2}}$. From figure 10(*b*) it follows that $(\overline{v'^2})^{\frac{1}{2}}$ is proportional to $x^{-\frac{1}{4}}$. s_γ should thus increase proportionally to the $\frac{1}{4}$ power of ξ'. As shown in figure 20, this is indeed the case. The increase of the standard deviation is related only to the geometric similarity in the far field and to the increase of the r.m.s. of the fluctuations of the lateral component of the velocity. The influence of the vortical structures and of the

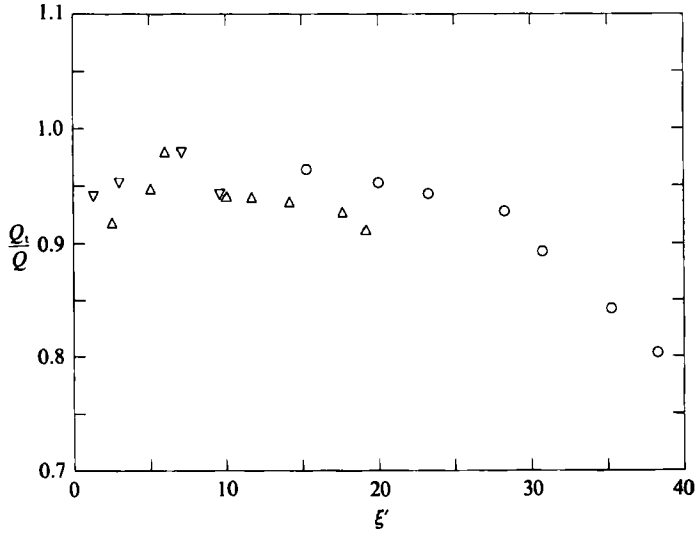

FIGURE 21. Ratio of turbulent to total discharge as a function of ξ'. Symbols as in figure 3.

quasi-two-dimensional turbulence is an indirect one and follows from the influence of the latter on the v-component of the velocity.

From the results presented in figure 20 the empirical equations relating $\eta_{0.5}$ and s_γ to ξ' are found to be

$$|\eta_{0.5}| = 7.5\,\xi'^{-\frac{1}{2}} \quad \text{valid for } \xi' > 20, \tag{12}$$

$$s_\gamma = 2\xi'^{\frac{1}{4}} \quad \text{valid for } \xi' > 10. \tag{13}$$

In the middle field, the distribution of γ in the transverse direction becomes skewed with long tails towards increasing $|\eta|$ values. Figure 19(b) shows this distribution at three locations in the range $5 < \xi' < 7$. The full lines correspond to lognormal distributions and fit the data satisfactorily. A significant shift of the γ-distributions away from the axis of the jet is observed in this range. The location of $\gamma = 0.5$ is namely $\eta_{0.5} = 1.85$ at $\xi' = 5$, $\eta_{0.5} = 2.05$ at $\xi = 6$ and $\eta_{0.5} = 1.95$ at $\xi' = 7$.

The intermittency function $I(t)$ also allows to determine the long time-average of the volume flux of turbulent fluid through a cross-section of the jet at a given position ξ' along its axis:

$$Q_t(\xi') = \int_{-\infty}^{+\infty} U_t(\xi', \eta)\,\mathrm{d}\eta. \tag{14}$$

The local average of the turbulent part of the velocity U_t can be computed by using (1), (12) and (13) from

$$U_t(\xi', \eta) = 2\int_0^\infty U_m(\xi')\,\mathrm{e}^{-A\eta^2}\left[1 - \frac{1}{(2\pi)^{\frac{1}{2}}\sigma_\gamma(\xi')}\int_{-\infty}^{\eta}\exp\left(-\frac{1}{2}\left(\frac{\eta - \eta_{0.5}(\xi')}{s_\gamma(\xi')}\right)^2\right)\mathrm{d}\eta\right]\mathrm{d}\gamma'. \tag{15}$$

The results of this calculation are presented in figure 21, in which the ratio Q_t/Q is plotted as a function of ξ'. Q is the total volume flux as determined from the profiles of the mean velocity. The deviation of the ratio Q_t/Q from unity indicates which part of the volume flux through a cross-section of a plane jet consists, on the average, of non-mixed entrained ambient fluid. In the near field the ratio Q_t/Q is somewhat smaller than 1 in all experiments with approximately 5% of the volume flux being non-turbulent. The contribution to non-turbulent flux comes mainly from the edges of the jet. Secondary currents seem to increase the transverse mixing efficiency in the midplane during their development. At $\xi' = 6$, where they are best developed, the ratio Q_t/Q reaches its maximum of 0.99. This is also consistent with the net increase

of turbulence intensity in this range shown in figure 10. In the range $H < \xi' < 10$, where the secondary currents start decaying, Q_t/Q decreases and reaches its initial value at $\xi' \approx 10$.

In the far field the ratio decreases monotonically, indicating that a considerable part (up to 20% at $\xi' = 38.25$) of the entrained fluid did not lose its irrotationality. The results of the intermittency analysis suggest that the development of the quasi-two-dimensional turbulence is the cause of the observed decrease of mixing efficiency in the far field.

9. Summary and conclusions

Plane turbulent jets discharging in shallow environment are studied up to a distance of approximately 40 times the depth of the receiving fluid body. The geometric and kinematic conditions imposed by the bounding surfaces influence the development of the jet in a distinct way. After a distance of about twice the depth H, and if the flow is well established, secondary currents start to develop. These currents induce weak helical flows with axes essentially parallel to the axis of the jet. Although too weak, these currents strongly influence the mean velocity distribution in the cross-section of the jet. The mean velocity distribution becomes three-dimensional, and this must be taken into account when balance equations are evaluated. The secondary currents also lead to an enhancement of turbulence and an increase of the mixing efficiency of fluid entrained by the jet. The maximum of the influence of the secondary currents is found at $\xi' \approx 6$, where $\xi' = x/H$. From that point the influence of these currents decreases and practically vanishes at $\xi' \approx 10$. The manner by which the secondary currents influence turbulence, intermittency and mixing is not yet completely understood and deserves further investigation.

The present study shows that two-dimensional large-amplitude quasi-periodic motions dominate the flow in the region beyond $\xi' \approx 10$. However, although the mean velocity profile and the spreading angle of the jet do not differ from the ones in the near field, e.g. for $\xi' < 2$, and are in accordance with the self-similarity of the jet, the structure of the flow undergoes a thorough change. Vorticity associated with the energy containing eddies aligns in a direction perpendicular to the bounding surfaces, giving rise to large-scale vortical coherent structures. The main stream in the jet appears to meander between these counter-rotating vortical structures, which grow in size with ξ' by pairing. The power spectra of turbulence start developing a range of quasi-two-dimensional turbulence, which initiates at the vicinity of the wavenumber corresponding to the beginning of the inertial subrange, and spreads towards lower wavenumbers with increasing ξ'. Nevertheless, the turbulence intensity of the u-component is constant in this region and fulfils similarity. The large structure behaviour produces an anisotropy of the r.m.s. values of u' and v'. The intermittency is strongly influenced by the large-scale structures of quasi-two-dimensional turbulence and so is the mixing efficiency of the jet. The latter is significantly reduced.

The authors thank Professor Dr A. Tsinober for his valuable comments and suggestions. This work was supported by the Swiss National Science Foundation, grant number 2.676-0.82. G.H.J. gratefully acknowledges support by the ETH Zurich during his sabbatical stay in Zurich, and additional support by the US National Science Foundation, grant number MSM-8806130, during preparation of the manuscript.

REFERENCES

ANTONIA, R. A., BROWNE, L. W. B., RAJAGOPALAN, S. & CHAMBERS, A. J. 1983 *J. Fluid Mech.* **134**, 49–66.

BASHIR, J. & UBEROI, M. S. 1975 *Phys. Fluids* **18**, 405–410.

BATCHELOR, G. K. 1969 *Phys. Fluids Suppl* II, 233–239.

BEVILAQUA, P. M. & LYKOUDIS, P. S. 1971 *AIAA J.* 9 (8), 1657–1659.

BRADBURY, L. J. S. 1965 *J. Fluid Mech.* **23**, 31–64.

CANTWELL, B. J. 1981 *Ann. Rev. Fluid Mech.* **13**, 457–515.

CERVANTES, J. G. 1981 Unsteady Turbulent Shear Flows, *IUTAM Symp. Toulouse*, pp. 412–424.

CERVANTES, J. G. & GOLDSCHMIDT, V. W. 1983 *Trans. ASME* I: *J. Fluids Engng* **103**, 119–126.

CORRSIN, S. & KISTLER, A. L. 1954 *Natl Adv. Ctee. Aero., Wash, Tech. Note* 3133.

DAVIES, A. E., KEFFER, J. F. & BAINES, W. D. 1975 *Phys. Fluids* **18**, 770–775.

DIMOTAKIS, P. E. & BROWN, G. L. 1976 *J. Fluid Mech.* **78**, 535–560.

EVERITT, K. W. & ROBINS, A. G. 1978 *J. Fluid Mech.* **88**, 563–583.

FOSS, J. F. 1977 *Proc. 1st Symp. Turbulent Shear Flows*, pp. 11.33-42.

FOSS, J. F. & JONES, J. B. 1968 *J. Basic Engng* 241–248.

GIGER, M. 1987 Doc. thesis ETH-Z, no. 8308.

GIGER, M., DRACOS, T. & JIRKA, G. H. 1991 *J. Hydraul. Res.* **29**, 615–641.

GOLDSCHMIDT, V. W. & BRADSHAW, P. 1981 *ASME Publ.* 81-FE-22, p. 7.

GOLDSCHMIDT, V. W., MOALLEMI, M. K. & OLER, J. W. 1983 *Phys. Fluids* **26**, 428–432.

GOLDSCHMIDT, V. W. & YOUNG, M. F. 1975 *4th Biennial Symp. on Turbulence in Liquids, Rolla, Missouri.*

GÖRTLER, H. 1942 *Z. angew Math. Mech.* **22**, 244–254.

GUTMARK, E. & WYGNANSKI, I. 1976 *J. Fluid Mech.* **73**, 465–495.

HESKESTAD, G. 1965 *J. Appl. Mech.* 721–734.

HOLDEMANN, J. D. & FOSS, J. F. 1975 *Trans ASME* I: *J. Fluids Engng* **111**, 342–352.

HUSSAIN, A. K. M. F. 1983 *Phys. Fluids* **26**, 2816–2850.

HUSSAIN, A. K. M. F. 1986 *J. Fluid Mech.* **173**, 303–356.

HUSSAIN, A. K. M. F. & ZEDAN, M. F. 1978 *Phys. Fluids* **21**, 1100–1112.

IKEDA, M. 1977 *J. Fluid Mech.* **80**, 401–421.

JIMENES, J. 1983 *J. Fluid Mech.* **132**, 319–336.

MICHALKE, A. & SCHADE, H. 1963 *Ingenieurarchiv* **33**, 1–23.

MOORE, D. W. & SAFFMAN, P. G. 1975 *J. Fluid Mech.* **69**, 465–473.

MOUM, J. N., KAWALL, J. G. & KEFFER, J. F. 1979 *Phys. Fluids* **22**, 1240–1244.

MOUM, J. N., KAWALL, J. G. & KEFFER, J. F. 1983 *Phys. Fluids* **26**, 2939–2945.

MÜLLER, A. 1980 *Proc. Symp. Long Range and Short Range Optical Velocity Measurements, German French res. Inst., Saint Louis, France*, R. 117/80, pp. XLII, 1–8.

MUMFORD, J. C. 1982 *J. Fluid Mech.* **118**, 241–268.

OLER, J. W. & GOLDSCHMIDT, V. W. 1982 *J. Fluid Mech.* **123**, 523–535.

PERKINS, H. J. 1970 *J. Fluid Mech.* **44**, 721–740.

RAMAPRIAN, B. R. & CHANDRASEKHARA, D. V. 1983 *IIHR Rep.* 257, University of Iowa, Iowa City, Iowa, USA.

REICHARDT, H. 1942 *VDI-Forschungsheft* 414.

SATO, H. 1960 *J. Fluid Mech.* **7**, 53–80.

TAYLOR, G. I. 1958 *J. Aero. Sci.* **25**, 464–465.

THOMAS, F. O. & GOLDSCHMIDT, V. W. 1986 *J. Fluid Mech.* **163**, 227–256.

TOLLMIEN, W. 1926 *Z. angew Math. Mech.* **6**, 468–478.

TOWNSEND, A. A. 1966 *J. Fluid Mech.* **26**, 689–715.

TOWNSEND, A. A. 1976 *The Structure of Turbulent Shear Flow.* Cambridge University Press.

WINANT, C. D. & BROWAND, F. K. 1974 *J. Fluid Mech.* **63**, 237–255.